

# Anisotropic light-matter interactions in the single-crystal topological insulator bismuth selenide

Divya Rawat , Aditya Singh , Niraj Kumar Singh , and Ajay Soni \*

*School of Physical Sciences, Indian Institute of Technology Mandi, Mandi 175005, Himachal Pradesh, India*



(Received 1 January 2023; revised 4 March 2023; accepted 3 April 2023; published 17 April 2023)

Anisotropy of light-matter interactions in materials gives remarkable information about phonons and their interactions with electrons. We report angle-resolved polarization Raman spectroscopy of single crystal of  $\text{Bi}_2\text{Se}_3$  to obtain elements of Raman tensor for understanding strength of polarization along different crystallographic orientations. Intensity variation in polar plots corresponding to  $E_g^1 \sim 37 \text{ cm}^{-1}$ ,  $A_{1g}^1 \sim 71 \text{ cm}^{-1}$ ,  $E_g^2 \sim 130 \text{ cm}^{-1}$ , and  $A_{1g}^2 \sim 173 \text{ cm}^{-1}$  suggests higher differential polarizability along the  $bc$  plane. The polar plots and elements of Raman tensor provide evidence of fundamental electron-phonon ( $e$ - $ph$ ) and anisotropic light-matter interactions in  $\text{Bi}_2\text{Se}_3$ .

DOI: [10.1103/PhysRevB.107.155203](https://doi.org/10.1103/PhysRevB.107.155203)

## I. INTRODUCTION

Light-matter interaction helps to understand the many-body physics and fundamentals of the electron and phonon coupling in materials [1,2]. Exploring the optical properties can provide significant understanding of (*an*)-isotropic interaction of light along with the electronic susceptibility and permittivity of the materials [3,4]. Generally, the electric field vector ( $\vec{E}$ ) of incident and scattered light are related through a complex matrix, known as Raman tensor ( $\vec{T}$ ) associated with the polarizability ( $\alpha$ ) of materials along three crystallographic orientations [5]. Recently, several materials such as  $\text{MoS}_2$  [5],  $\text{WS}_2$  [6],  $\text{MoSe}_2$  [5], and  $\text{PdSe}_2$  [7] have been studied using Raman spectroscopy by controlling the polarization vector of incident and scattered light, to understand dynamics of phonons along the different orientation of the crystal. Chalcogenide materials have been known for their anisotropic carrier relaxation times, which mainly arises due to their intriguing crystal structures and inherent anharmonicity [8,9]. Additionally, Raman studies on ternary chalcogenides,  $\text{Bi}_2\text{GeTe}_4$ ,  $\text{Sb}_2\text{SnTe}_4$  have shown that electronic topological properties can also be coupled with phonons, which is shown by the anomalous thermal behavior of Raman modes [9]. Although several chalcogenide quantum materials have been explored extensively for their exotic electronic phenomena, such as  $\text{Sd-H}$  oscillations [10], weak (anti)localization [11], thermoelectricity, superconductivity, charge-density waves, and topological insulating properties, the coupling of topological electrons with phonons is yet less explored [12–14].  $\text{Bi}_2\text{Se}_3$  is one of the layered chalcogenides which has a fascinating layered crystal structure of five atoms (quintuple layers) stacked with van der Waals gaps [15]. Primarily, the topological studies on  $\text{Bi}_2\text{Se}_3$  have a focus on investigating surface and bulk electronic structures using magnetotransport and angle-resolved polarization Raman spectroscopy (APRS) studies, phonon dispersion [16–18], but there are imperceptible reports on the anisotropic response of the inelastic light scattering. Since the topological phenomena are associated with electrons,  $e$ - $ph$ ,

and electron-photon interactions [4,19], thus the investigation of the anisotropy of the electron-phonon-photon interaction, dynamics of phonon, and evaluation of Raman tensor are very important to explore. In this regard, APRS can provide a significant information about light-sensitive responses of single crystals along various orientations by controlling the polarization of both incident and scattered photons to acquire the evidences of  $e$ - $ph$  interactions and anisotropic behavior [20]. Here, we have discussed APRS to corroborate the interaction between the polarized light ( $k_i$ ) and the crystallographic orientation of  $\text{Bi}_2\text{Se}_3$ . The anisotropic behavior of modes are studied with the rotation of crystal along two different configurations in the  $ab$  plane ( $k_i \parallel c$  axis) and  $bc$  plane ( $k_i \parallel a$  axis), respectively. The observed anisotropic behavior and polarizability of in-plane ( $E_g$ ) and out-of-plane ( $A_{1g}$ ) modes are quantified from the Raman tensor's elements. Our results open the prospects to understand the anisotropic light-matter and  $e$ - $ph$  interactions by both classical as well as quantum treatment of Raman tensors obtained from APRS analysis. Experimental details of synthesis and characterization of the single crystal are mentioned in the Supplemental Material (SM) [21].

## II. RESULTS AND DISCUSSIONS

The layered nature of grown  $\text{Bi}_2\text{Se}_3$  is shown in the field-emission scanning electron microscopy image [Fig. 1(a)] and the x-ray-diffraction (XRD) pattern in Fig. 1(b), which confirms the orientation of the grown sample along  $c$  axis [22]. Rietveld refinement of the XRD pattern of powdered  $\text{Bi}_2\text{Se}_3$  provides the lattice parameters  $a = b \sim 4.13 \text{ \AA}$ ,  $c \sim 28.63 \text{ \AA}$ , and unit-cell volume ( $V$ )  $\sim 425 \text{ \AA}^3$  (Fig. S1, SM [21]). The residual resistance ratio (RRR $\sim 2.11$ ) has been evaluated from the low-temperature resistance measurement (Fig. S2, SM [21]) which shows a generated electron transport in a high-quality single crystal [21,23].  $\text{Bi}_2\text{Se}_3$  crystallizes in a rhombohedral structure with space group  $R\bar{3}m$  (166), which comprised of quintuple layers ( $\text{Se}^I$ - $\text{Bi}$ - $\text{Se}^{II}$ - $\text{Bi}$ - $\text{Se}^I$ ) separated by weak van der Waals gap [Fig. 1(c)]. Here,  $\text{Se}^I$  and  $\text{Se}^{II}$  represent different chemical environment of Se atoms in unit cell [24,25]. The primitive unit cell of  $\text{Bi}_2\text{Se}_3$  has 15 zone-center vibrational modes, 3 acoustic and 12 optical, which can be represented by

\* [ajay@iitmandi.ac.in](mailto:ajay@iitmandi.ac.in)

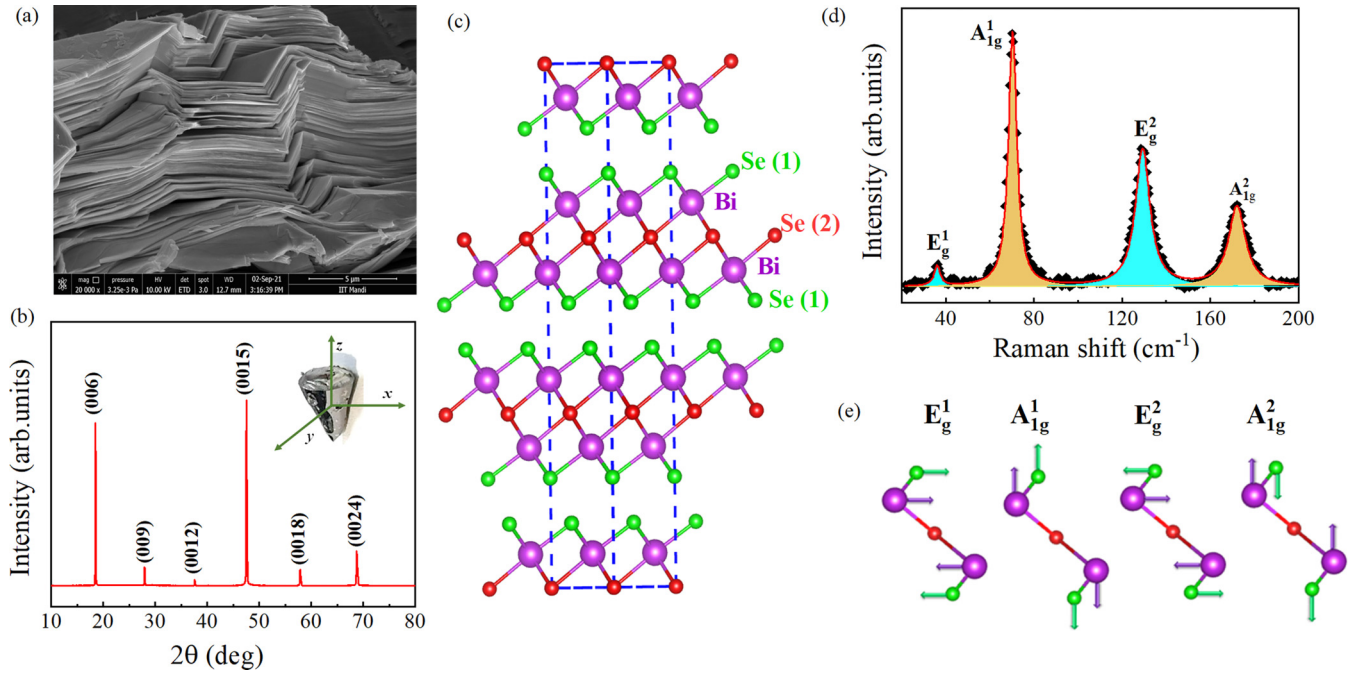


FIG. 1. (a) Microscopy image of cross section of  $\text{Bi}_2\text{Se}_3$ , (b) XRD pattern of single crystal showing typical orientation along  $c$  axis. (Inset) Photograph of sample. (c) Schematic of crystal structure comprises quintuple layers; (d) Raman spectra; and (e) schematic of atomic displacements of  $E_g$  and  $A_{1g}$  modes.

$\Gamma = 2E_g + 2A_{1g} + 2E_u + 2A_{1u}$ , where  $A_{1g}$  and doubly degenerate  $E_g$  are Raman-active modes, whereas  $2A_{1u}$  and  $2E_u$  are the infrared active modes [25]. Normalized Raman spectra, having modes at  $\sim 37 \text{ cm}^{-1}$  ( $E_g^1$ ),  $\sim 71 \text{ cm}^{-1}$  ( $A_{1g}^1$ ),  $\sim 130 \text{ cm}^{-1}$  ( $E_g^2$ ), and  $\sim 173 \text{ cm}^{-1}$  ( $A_{1g}^2$ ), is shown in Fig. 1(d) and the corresponding atomic displacements are illustrated in Fig. 1(e). The modes  $A_{1g}^1$  ( $A_{1g}^2$ ) and  $E_g^1$  ( $E_g^2$ ) have a different polarizability as they involve out-of-plane and in-plane displacements in symmetric (antisymmetric) stretching, respectively. Thus, APRS is an important tool to provide the detailed information on the interaction of the light along the different orientations of crystal for estimation of Raman tensor.

Figure 2 represents the two configurations used for the APRS measurements, where crystallographic axes  $a$ ,  $b$ , and  $c$  are taken as equivalent to  $x$ ,  $y$ , and  $z$  axes of rotating stage. For the first configuration [Fig. 2(a)], the incident laser ( $k_i$ ) is parallel to the  $c$  axis, and the electric polarization vector ( $e_i$ ) is making an angle  $\omega$  with the  $a$  axis (in the  $ab$  plane). Hence, the scattering configuration is defined as  $z(xx)\bar{z}$ , and the corresponding polarization vectors of incident and scattered light are  $\vec{e}_i = \vec{e}_s = (\cos \omega, \sin \omega, 0)$ . For the second configuration [Fig. 2(b)], the incident  $k_i$  is parallel to the  $a$  axis and  $e_i$  is making an angle  $\theta$  with the  $b$  axis (in the  $bc$  plane). Correspondingly, the scattering configuration is defined as  $x(yy)\bar{x}$  and the polarization vectors of incident and scattered light are  $\vec{e}_i = \vec{e}_s = (0, \cos \theta, \sin \theta)$ . Being isotropic in the  $ab$  plane,  $\text{Bi}_2\text{Se}_3$  crystal does not have any changes in intensity along the  $a$  and  $b$  axes while the light-matter interactions are anisotropic along the  $c$  axis and a detailed Raman tensor is not reported.

Polarized Raman spectra with the rotation of crystal along both the  $ab$ (/ $bc$ )-planes and corresponding color plot is shown in Fig. 3. The intensity of  $A_{1g}^1$  ( $A_{1g}^2$ ) and  $E_g^1$  ( $E_g^2$ ) modes are not changing along the  $ab$ -plane [Fig. 3(a)], whereas a periodic

alteration has been observed along the  $bc$  plane [Fig. 3(b)]. The results indicate that there is an existence of anisotropy along the  $bc$  plane as compared to the  $ab$  plane, which can be examined clearly from polar plots. We have also studied the anisotropic Raman scattering with the 633- and 785-nm laser excitation, which showed different polar pattern of Raman modes (Fig. S3, Supplemental Material [21]). According to

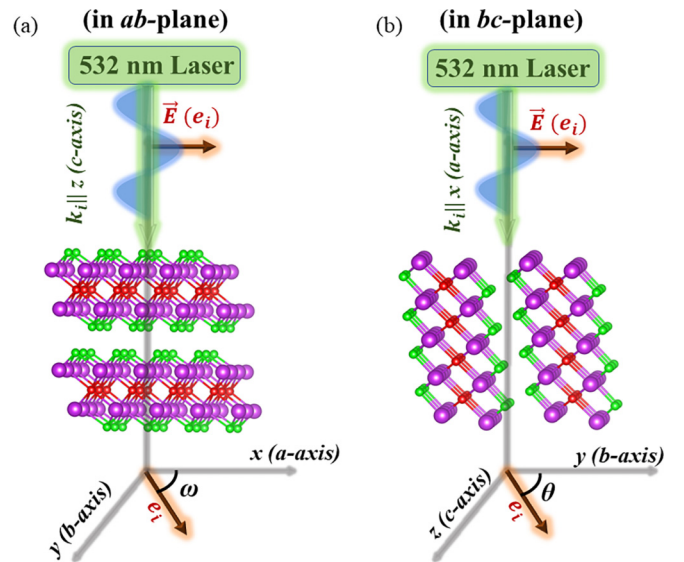


FIG. 2. Schematic representation of the two configurations used for APRS studies, where polarized laser ( $k_i$ ) incidents along (a)  $c$  axis (on  $ab$  plane) and (b) normal to  $c$  axis ( $bc$  plane). Here,  $\omega$  and  $\theta$  correspond to the angle between electric polarization vector ( $e_i$ ) of incident light with  $a$  axis (in  $ab$  plane) and  $b$  axis (in  $bc$  plane), respectively.

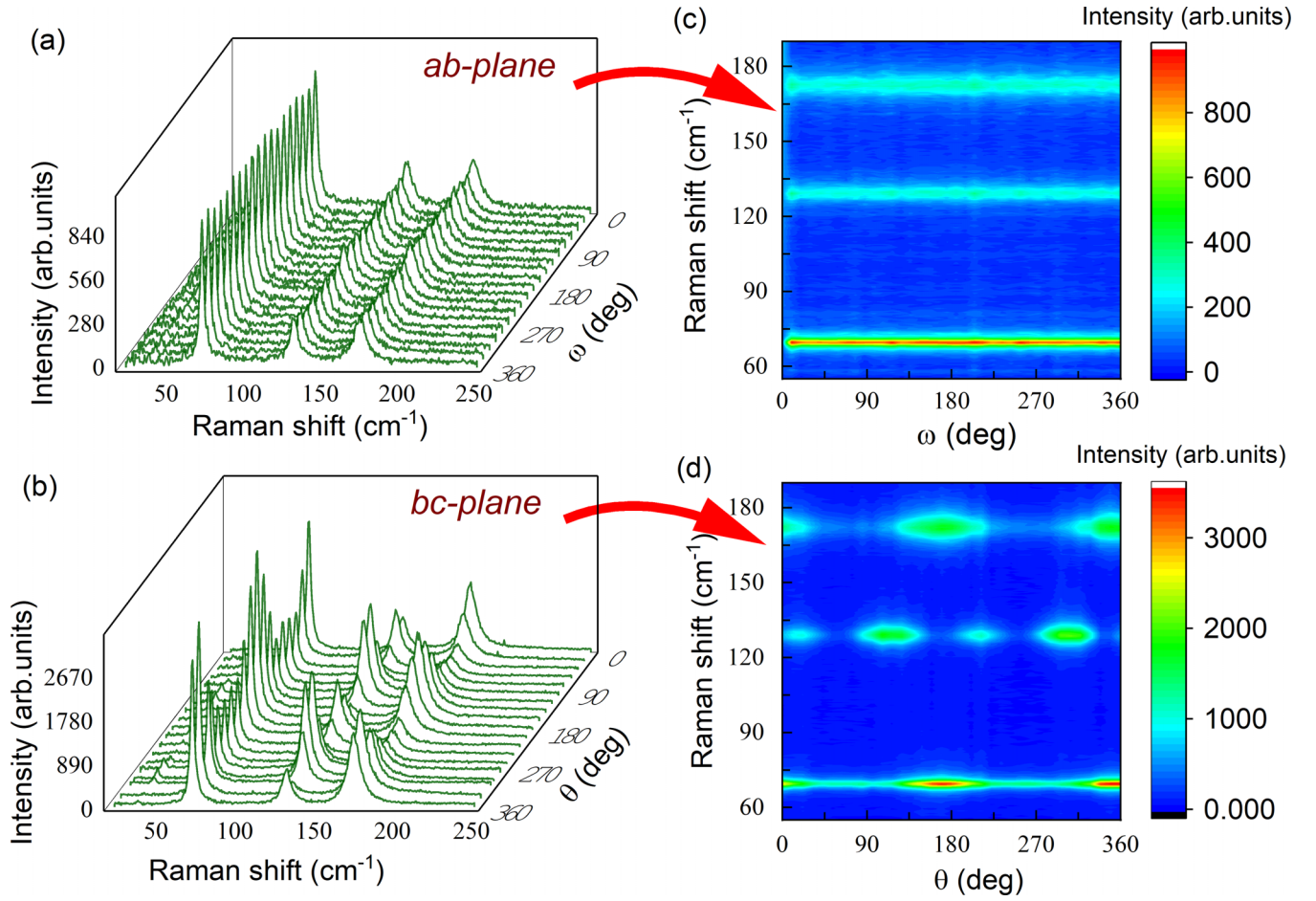


FIG. 3. Angle-dependent polarized Raman spectra (a), (b) and corresponding polarized Raman color plot with the rotation of the  $\text{Bi}_2\text{Se}_3$  sample in parallel configuration of polarized incident ( $e_i$ ) and scattered ( $e_s$ ) light along  $ab$  as well as  $bc$  plane. Color scale on the right side shows the intensity variation of Raman modes.

classical treatment of Raman tensor, the inelastic processes can be explained by the scattering from an extended medium, where the variations of the polarization can be expressed as a derivative of the susceptibility of materials [20]. The contribution of spatial symmetry to the Raman-scattering intensity ( $I$ ) can be expressed as  $\langle e_i | \mathbb{T} | e_s \rangle^2$ , where  $\mathbb{T}$  is the Raman tensor for a given mode [25]. Thus, the elements of Raman tensor of  $A_{1g}$  and double-degenerate  $E_g$  modes can be represented as

$$\mathbb{T}(A_{1g}) = \begin{bmatrix} \eta e^{i\theta_\eta} & 0 & 0 \\ 0 & \eta e^{i\theta_\eta} & 0 \\ 0 & 0 & \beta e^{i\theta_\beta} \end{bmatrix},$$

$$\mathbb{T}(E_g) = \begin{bmatrix} \gamma e^{i\theta_\gamma} & 0 & 0 \\ 0 & -\gamma e^{i\theta_\gamma} & \delta e^{i\theta_\delta} \\ 0 & \delta e^{i\theta_\delta} & 0 \end{bmatrix};$$

$$\begin{bmatrix} 0 & -\gamma e^{i\theta_\gamma} & -\delta e^{i\theta_\delta} \\ -\gamma e^{i\theta_\gamma} & 0 & 0 \\ -\delta e^{i\theta_\delta} & 0 & 0 \end{bmatrix}.$$

Here, values corresponding to  $\eta$ ,  $\beta$ ,  $\gamma$ , and  $\delta$  indicate amplitudes whereas  $\theta_\eta$ ,  $\theta_\beta$ ,  $\theta_\gamma$ , and  $\theta_\delta$  are the complex phases

of elements of Raman tensor [20]. Additionally, the magnitude of each tensor element is related with the specific mode and the crystal symmetry of the material. The calculated intensities for the estimation of the  $\mathbb{T}(E_g)$  has contributions from both the doubly degenerate  $E_g$  modes, thus added altogether. Using the Raman selection rule,  $|\langle e_i | \mathbb{T}^* | e_s \rangle|^2$ , under both  $ab(bc)$ -planes, the scattering intensity of all modes have been calculated (Table I), which clearly showed the distinct strength of interaction of polarized light with the crystal's axes [5,26,27].

Further, the understanding of the isotropic behavior along the  $ab$  plane of the intensity of  $A_{1g}$  and  $E_g$  modes are depicted as circular shapes of the polar intensity plots [Figs. 4(a) and 4(b)]. On the other hand, the shape of polar plots for  $A_{1g}$  [Figs. 4(c) and 4(d)] and  $E_g$  [Figs. 4(e) and 4(f)] modes along the  $bc$  plane are different from the  $ab$  plane showing the anisotropy of the light-matter interaction along crystallographic orientation. The intensities of all modes are stronger along the  $bc$  plane in comparison to the  $ab$  plane, which advocates the higher differential polarizability along the  $bc$  plane. Similar observations on the anisotropic light-matter interaction in the  $bc$  plane have been reported for Graphene, hBN, 2H-MoSe<sub>2</sub>, and MoS<sub>2</sub> [5,28]. Out-of-plane modes at  $\sim 71 \text{ cm}^{-1}$  and  $\sim 173 \text{ cm}^{-1}$  [Figs. 4(c) and 4(d)] have

TABLE I. Mathematically derived intensity of modes using Raman selection rules.

S. no.	Configuration	Raman-scattering intensity
1.	<i>ab</i> plane	$I_{A_{1g}}^{\parallel} (k_i \parallel c \text{ axis}) =  \eta ^2$ $I_{E_g}^{\parallel} (k_i \parallel c \text{ axis}) =  \gamma ^2$
2.	<i>bc</i> plane	$I_{A_{1g}}^{\parallel} (k_i \parallel c \text{ axis}) =  \eta ^2 \sin^4 \theta +  \beta ^2 \cos^4 \theta + \frac{1}{2}  \eta   \beta  \sin^2(2\theta) \cos \varphi_{\eta\beta}$ $I_{E_g}^{\parallel} (k_i \parallel a \text{ axis}) =  \gamma ^2 \cos^4 \theta +  \delta ^2 \sin^2 2\theta -  \delta   \gamma  \sin(2\theta) \cos^2 \theta \times 2 \cos \varphi_{\gamma\delta}$

$A_{1g}$  symmetry but show considerably different polar pattern at  $90^\circ$  and  $270^\circ$  rotations. The anomalous polarization dependence of the Raman intensities appeared because of difference in Raman-scattering cross section through the second-order susceptibility or the electron-phonon (*e-ph*) interactions [20].

To understand this discrepancy, the microscopic quantum description of Raman tensor, which involved the *e-ph* interaction in addition to the electron-photon, has been adopted [29]. Here, the total Raman intensity is described by the product of both the electron-photon and *e-ph* interactions. Hence, the Raman tensor ( $\mathbb{T}_{ij}^k$ ) associated with all modes can be given by

$$\mathbb{T}_{ij}^k = \frac{1}{V} \sum_{v,c,c'} \sum_{q'} \frac{\langle \Psi v(\vec{q}) | \vec{e}_s \cdot \vec{\nabla} | \Psi_{c'}(\vec{q}) \rangle \langle \Psi_{c'}(\vec{q}) | H_{ep}^k | \Psi_c(\vec{q}) \rangle \langle \Psi_c(\vec{q}) | \vec{e}_i \cdot \vec{\nabla} | \Psi v(\vec{q}) \rangle}{(E_L - E_{cv}(\vec{q}) - i\Gamma_c)(E_L - \hbar\omega_{ph}^k - E_{c'v}(\vec{q}) - i\Gamma_{c'})}$$

Here, the numerator consists of the product of three matrix elements, (i) the *e-ph* matrix elements ( $\langle \Psi_{c'}(\vec{q}) | H_{ep}^k | \Psi_c(\vec{q}) \rangle$ ) and two electron-photon matrix elements for incident and scattered light, (ii) ( $\langle \Psi_{c'}(\vec{q}) | \vec{e}_i \cdot \vec{\nabla} | \Psi v(\vec{q}) \rangle$ ), (iii) ( $\langle \Psi v(\vec{q}) | \vec{e}_s \cdot \vec{\nabla} | \Psi_{c'}(\vec{q}) \rangle$ ), where  $\vec{e}_i$  and  $\vec{e}_s$  are the polarization vectors of incident and scattered light, respectively [29]. The summation is over the electronics branches in conduction ( $c$ ,  $c'$ ) and valence ( $v$ ) bands along with all wave vectors with first Brillouin zone.  $\Gamma_c$  and  $\Gamma_{c'}$  are the broadening factor associated with the lifetime of photoexcited states. The inclusion of *e-ph* matrix element gives the major differences among both the out-of-plane  $A_{1g}$  modes. Thus, different patterns of polar plots for  $A_{1g}^1$  and  $A_{1g}^2$  modes indicate *e-ph* interactions in  $\text{Bi}_2\text{Se}_3$ , similar to the observations in other chalcogenides like  $\text{WS}_2$ ,  $\text{GaTe}$ ,  $\text{ReSe}_2$ ,  $\text{ReS}_2$ , and black phosphorus [6,20,29–32]. In contrast to the  $A_{1g}$  modes, the polar plots of  $E_g$  modes show four-lobed polar pattern [Figs. 4(e) and 4(f)] with

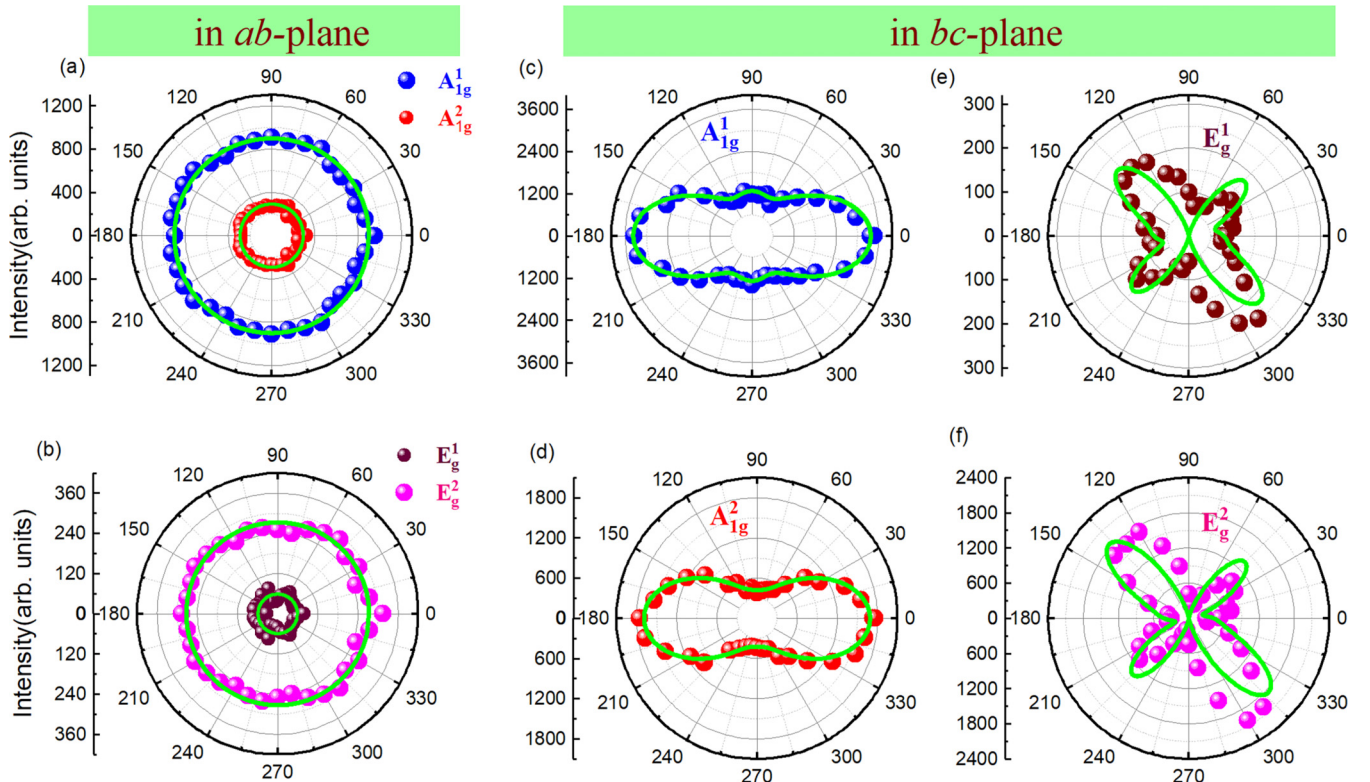


FIG. 4. Intensities of polar plots for  $A_{1g}^1$ ,  $A_{1g}^2$ ,  $E_g^1$ , and  $E_g^2$  modes in *ab* plane (a), (b), and in *bc* plane (c)–(f). Here, solid symbols and green line represent the experimental data and fitting of the data using equation in Table I, respectively.

TABLE II. Estimated Raman tensor elements obtained from the fitting of experimental data (Fig. 4).

Modes	Raman tensor					
	<i>ab</i> plane			<i>bc</i> plane		
$A_{1g}^1$	$\begin{bmatrix} 30 & 0 & 0 \\ 0 & 30 & 0 \\ 0 & 0 & \beta \end{bmatrix}$	$\begin{bmatrix} 35 & 0 & 0 \\ 0 & 35 & 0 \\ 0 & 0 & 57e^{i0.37\pi} \end{bmatrix}$				
$A_{1g}^2$	$\begin{bmatrix} 17 & 0 & 0 \\ 0 & 17 & 0 \\ 0 & 0 & \beta \end{bmatrix}$	$\begin{bmatrix} 21 & 0 & 0 \\ 0 & 21 & 0 \\ 0 & 0 & 41e^{i0.24\pi} \end{bmatrix}$				
$E_g^1$	$\begin{bmatrix} 8 & -8 & \delta \\ -8 & -8 & \delta \\ \delta & \delta & 0 \end{bmatrix}$	$\begin{bmatrix} 8 & -8 & -13e^{i0.39\pi} \\ -8 & -8 & 13e^{i0.39\pi} \\ -13e^{i0.39\pi} & 13e^{i0.39\pi} & 0 \end{bmatrix}$				
$E_g^2$	$\begin{bmatrix} 16 & -16 & \delta \\ -16 & -16 & \delta \\ \delta & \delta & 0 \end{bmatrix}$	$\begin{bmatrix} 14 & -14 & -38e^{i0.32\pi} \\ -14 & -14 & 38e^{i0.32\pi} \\ -38e^{i0.32\pi} & 38e^{i0.32\pi} & 0 \end{bmatrix}$				

the rotation of the crystal, which indicates the maximum strength of anisotropic nature in the *bc* plane. However, there are no such changes on the phonon frequency and linewidth of these modes with the rotation of crystal along the *bc* plane (Figs. S4(a) and S4(b) [21]). To understand the behavior of polar plots related to  $E_g$  modes, the spectra have been captured by controlling the polarization of incident light ( $e_i$ ). This configuration is done by rotating half wave plate from  $0^\circ$  to  $360^\circ$  while keeping the sample stage and analyzer fixed (Fig. S5 [21]). Here, the intensity of both  $A_{1g}$  modes (Figs. S5(a) and S5(b) [21]) showed analogous polar pattern with polarization angle, whereas  $E_g$  modes (Fig. S5(c) [21]) exhibited a low dependency on the rotation of the half wave plate. This discrepancy of the  $E_g$  modes between the rotation of crystallographic axis and incident laser suggest the anisotropic behavior along the *bc* plane [5]. Anisotropic light-matter interaction has been understood by estimating the amplitude and phase difference of Raman tensor's element, which mainly contain the information of differential polarizability along different orientation. To estimate the Raman tensor elements of all modes, we have fitted the experimental data (in Fig. 4) using the intensity's expressions given in Table I and the obtained details are presented in Table II.

In the *ab* plane, all modes show isotropic behavior [Figs. 4(a) and 4(b)]; hence, for  $\mathbb{T}$  ( $A_{1g}$ ) and  $\mathbb{T}$  ( $E_g$ ), the component of Raman tensor,  $\eta$  ( $A_{1g}^1 \sim 30$  and  $A_{1g}^2 \sim 17$ ) and  $\gamma$  ( $E_g^1 \sim 8$  and  $E_g^2 \sim 16$ ), have been evaluated from the fitting of polar plots. As incident light ( $k_i$ ) is along the *c* axis, there

is no polarization along the *c* axis; thus,  $\beta$  for  $A_{1g}$  mode is not evaluated while  $\beta$  is zero for  $E_g$  modes. Here, phase factor ( $\vartheta_\eta$ ) is zero due to isotropic responses in the *ab* plane. In the *bc* plane [Figs. 4(c) and 4(d)], component of Raman tensor,  $\eta$  ( $A_{1g}^1 \sim 35$  and  $A_{1g}^2 \sim 21$ ) and  $\beta$  ( $A_{1g}^1 \sim 57$  and  $A_{1g}^2 \sim 41$ ) have been evaluated and phase factor between  $\eta$  and  $\beta$  ( $\vartheta_{\eta\beta}$ ) is  $\sim 67.3^\circ$  ( $0.37\pi$ ) for  $A_{1g}^1$  and  $\sim 44^\circ$  ( $0.24\pi$ ) for  $A_{1g}^2$ , which is arising due to the anisotropic responses. Additionally, the elements of Raman tensor for in-plane modes are  $\gamma$  ( $E_g^1 \sim 8$  and  $E_g^2 \sim 14$ ) and  $\delta$  ( $E_g^1 \sim 13$  and  $E_g^2 \sim 38$ ) and the phase factor between  $\gamma$  and  $\delta$  ( $\vartheta_{\gamma\delta}$ ) is  $\sim 71^\circ$  ( $0.39\pi$ ) for  $E_g^1$  and  $\sim 58.4^\circ$  ( $0.32\pi$ ) for  $E_g^2$ . For out-of-plane  $A_{1g}$  modes,  $\beta > \eta$ , ( $57 > 35$  for  $A_{1g}^1$  and  $41 > 21$  for  $A_{1g}^2$ ), which indicates that differential polarizability is significantly higher and anisotropic along the *c* axis. By comparing the tensor matrices of out-of-plane modes, it is evident that symmetric stretching ( $A_{1g}^1$ ) induces higher polarizability than antisymmetric stretching ( $A_{1g}^2$ ) and the situation is completely otherwise for in-plane modes  $E_g^1$  and  $E_g^2$  as confirmed by smaller magnitude of Raman tensor elements (Table II). For both *ab*- and *bc* planes, the comparison of relative magnitude of Raman tensor elements of  $A_{1g}^1$  ( $|\eta_{bc\text{-plane}}/\eta_{ab\text{-plane}}| \sim 1.16$ ) and  $E_g^2$  ( $|\gamma_{ab\text{-plane}}/\gamma_{bc\text{-plane}}| \sim 1.14$ ), which authenticate the estimated elements of Raman tensor, which is valid for 532-nm laser [5]. Comparing the APRS estimated Raman tensor elements with studies on MoSe<sub>2</sub>, MoS<sub>2</sub>, WSe<sub>2</sub>, and PdTe<sub>2</sub>, it is clear that APRS demonstrates the anisotropic light-matter interactions in Bi<sub>2</sub>Se<sub>3</sub>.

### III. CONCLUSIONS

In summary, Raman tensor for all modes of single-crystal Bi<sub>2</sub>Se<sub>3</sub> corresponds to  $E_g^1 \sim 37\text{ cm}^{-1}$ ,  $A_{1g}^1 \sim 70\text{ cm}^{-1}$ ,  $E_g^2 \sim 129\text{ cm}^{-1}$ , and  $A_{1g}^2 \sim 172\text{ cm}^{-1}$  have been systematically studied by APRS along both *ab*(/*bc*)-planes under parallel polarization ( $e_i \parallel e_s$ ) scattering configuration. We have estimated amplitude and phase difference of the tensor elements by fitting the polar plots with the intensity expression obtained using Raman selection rule. Different shapes of polar plot of the similar vibrational symmetry ( $A_{1g}$ ) represents the different interaction of electrons with phonons, which provide the evidence of *e-ph* coupling. Among two different orientations [*ab*(/*bc*)-planes], strong polarization dependence has been observed along the *bc* planes for both  $A_{1g}$  and  $E_g$  modes, which shows the anisotropic light-matter interaction in Bi<sub>2</sub>Se<sub>3</sub>.

### ACKNOWLEDGMENT

We thank IIT Mandi for instruments and research facilities and acknowledge DST-SERB for funding (Grant No. CRG/2018/002197).

- [1] C. Grazianetti, C. Martella, and E. Cinquanta, *Opt. Mater.: X* **12**, 100088 (2021).  
 [2] Y. Xu, D. Ji, H. Song, N. Zhang, Y. Hu, T. D. Anthopoulos, E. M. Di Fabrizio, S. Xiao, and Q. Gan, *Adv. Opt. Mater.* **6**, 1800444 (2018).

- [3] J. Singh, *Optical Properties of Condensed Matter and Applications* (John Wiley & Sons, Hoboken, NJ, 2006), Vol. 6.  
 [4] Y. Xia, D. Qian, D. Hsieh, L. Wray, A. Pal, H. Lin, A. Bansil, D. Grauer, Y. S. Hor, R. J. Cava, and M. Z. Hasan, *Nat. Phys.* **5**, 398 (2009).

- [5] Y. Ding, W. Zheng, M. Jin, Y. Zhu, R. Zhu, Z. Lin, and F. Huang, *Opt. Lett.* **45**, 1313 (2020).
- [6] Y. Ding, W. Zheng, Z. Lin, R. Zhu, M. Jin, Y. Zhu, and F. Huang, *Sci. China Mater.* **63**, 1848 (2020).
- [7] A. A. Puretzy, A. D. Oyedele, K. Xiao, A. V. Haglund, B. G. Sumpter, D. Mandrus, D. B. Geohegan, and L. Liang, *2D Mater.* **5**, 035016 (2018).
- [8] J. P. Heremans, *Nat. Phys.* **11**, 990 (2015).
- [9] N. K. Singh, D. Rawat, D. Dey, A. Elsukova, P. O. Å. Persson, P. Eklund, A. Taraphder, and A. Soni, *Phys. Rev. B* **105**, 045134 (2022).
- [10] Z. Ren, A. A. Taskin, S. Sasaki, K. Segawa, and Y. Ando, *Phys. Rev. B* **82**, 241306(R) (2010).
- [11] N. K. Singh, A. Kashyap, and A. Soni, *Appl. Phys. Lett.* **119**, 223903 (2021).
- [12] S. Acharya, J. Pandey, and A. Soni, *Appl. Phys. Lett.* **109**, 133904 (2016).
- [13] J. E. Moore, *Nature (London)* **464**, 194 (2010).
- [14] J. Pandey and A. Soni, *Phys. Rev. Res.* **2**, 033118 (2020).
- [15] W. Richter and C. R. Becker, *Phys. Status Solidi B* **84**, 619 (1977).
- [16] A. C. Ferrari and D. M. Basko, *Nat. Nanotechnol.* **8**, 235 (2013).
- [17] S. R. Park, J. Han, C. Kim, Y. Y. Koh, C. Kim, H. Lee, H. J. Choi, J. H. Han, K. D. Lee, N. J. Hur *et al.*, *Phys. Rev. Lett.* **108**, 046805 (2012).
- [18] S. Sharma, S. Kumar, G. C. Tewari, G. Sharma, E. F. Schwier, K. Shimada, A. Taraphder, and C. S. Yadav, *Phys. Rev. B* **105**, 115120 (2022).
- [19] M. Z. Hasan and C. L. Kane, *Rev. Mod. Phys.* **82**, 3045 (2010).
- [20] J. Kim, J.-U. Lee, and H. Cheong, *J. Phys.: Condens. Matter* **32**, 343001 (2020).
- [21] See Supplemental Material at <http://link.aps.org/supplemental/10.1103/PhysRevB.107.155203> for synthesis, characterization, and excitation laser dependence.
- [22] K. Mazumder and P. M. Shirage, *J. Alloys Compd.* **888**, 161492 (2021).
- [23] T. Kino, T. Endo, and S. Kawata, *J. Phys. Soc. Jpn.* **36**, 698 (1974).
- [24] A. Soni, Z. Yanyuan, Y. Ligen, M. K. K. Aik, M. S. Dresselhaus, and Q. Xiong, *Nano Lett.* **12**, 1203 (2012).
- [25] J. Zhang, Z. Peng, A. Soni, Y. Zhao, Y. Xiong, B. Peng, J. Wang, M. Dresselhaus, and Q. Xiong, *Nano Lett.* **11**, 2407 (2011).
- [26] Y. Ding, W. Zheng, X. Lu, Y. Liang, Y. Zhu, M. Jin, and F. Huang, *J. Phys. Chem. Lett.* **11**, 10094 (2020).
- [27] J. R. Ferraro, K. Nakamoto, and C. W. Brown, in *Introductory Raman Spectroscopy*, edited by J. R. Ferraro, K. Nakamoto, and C. W. Brown (Academic Press, San Diego, 2003), p. 1.
- [28] J. Ribeiro-Soares, R. M. Almeida, E. B. Barros, P. T. Araujo, M. S. Dresselhaus, L. G. Cançado, and A. Jorio, *Phys. Rev. B* **90**, 115438 (2014).
- [29] G. C. Resende, G. A. Ribeiro, O. J. Silveira, J. S. Lemos, J. C. Brant, D. Rhodes, L. Balicas, M. Terrones, M. S. Mazzoni, and C. Fantini, *2D Mater.* **8**, 025002 (2020).
- [30] S. Huang, Y. Tatsumi, X. Ling, H. Guo, Z. Wang, G. Watson, A. A. Puretzy, D. B. Geohegan, J. Kong, and J. Li, *ACS Nano* **10**, 8964 (2016).
- [31] X. Ling, S. Huang, E. H. Hasdeo, L. Liang, W. M. Parkin, Y. Tatsumi, A. R. T. Nugraha, A. A. Puretzy, P. M. Das, B. G. Sumpter *et al.*, *Nano Lett.* **16**, 2260 (2016).
- [32] S. Zhang, N. Mao, N. Zhang, J. Wu, L. Tong, and J. Zhang, *ACS Nano* **11**, 10366 (2017).